The Astrophysical Journal, 823:80 (8pp), 2016 June 1 doi:10.3847/0004-637X/823/2/80

DUST COAGULATION IN THE VICINITY OF A GAP-OPENING JUPITER-MASS PLANET

Augusto Carballido, Lorin S. Matthews, and Truell W. Hyde
Center for Astrophysics, Space Physics and Engineering Research, Baylor University, Waco, TX 76798, USA; Augusto_Carballido@baylor.edu
Received 2015 November 30; accepted 2016 March 24; published 2016 May 25

ABSTRACT

We analyze the coagulation of dust in and around a gap opened by a Jupiter-mass planet. To this end, we carry out a high-resolution magnetohydrodynamic (MHD) simulation of the gap environment, which is turbulent due to the magnetorotational instability. From the MHD simulation, we obtain values of the gas velocities, densities, and turbulent stresses (a) close to the gap edge, (b) in one of the two gas streams that accrete onto the planet, (c) inside the low-density gap, and (d) outside the gap. The MHD values are then input into a Monte Carlo dust-coagulation algorithm which models grain sticking and compaction. We also introduce a simple implementation for bouncing, for comparison purposes. We consider two dust populations for each region: one whose initial size distribution is monodisperse, with monomer radius equal to 1 μm, and another one whose initial size distribution follows the Mathis–Rumpl–Nordsieck distribution for interstellar dust grains, with an initial range of monomer radii between 0.5 and 10 μm. Without bouncing, our Monte Carlo calculations show steady growth of dust aggregates in all regions, and the mass-weighted (m-w) average porosity of the initially monodisperse population reaches extremely high final values of 98%. The final m-w porosities in all other cases without bouncing range between 30% and 82%. The efficiency of compaction is due to high turbulent relative speeds between dust particles. When bouncing is introduced, growth is slowed down in the planetary wake and inside the gap. Future studies will need to explore the effect of different planet masses and electric charge on grains.

Key words: magnetohydrodynamics (MHD) – planet–disk interactions – planets and satellites: formation – protoplanetary disks – turbulence

1. INTRODUCTION

Recent images of several distinct gaps and rings in the disk around HL Tau (ALMA Partnership et al. 2015) have led to calls for caution when interpreting the origin of such structures in protoplanetary disks. While imaging studies have shown that gaps can be associated with protoplanets (Kraus & Ireland 2012; Quanz et al. 2015), it has also been demonstrated that apparent gaps can be produced by the accumulation of millimeter-sized dust particles in narrow rings as a result of dust growth and pile-ups (Gonzalez et al. 2015a). The role of dust in interpreting images of disks with gaps, therefore, should not be overlooked.

Numerical investigations of the dynamics of dust particles in the neighborhood of a gap-opening planet reveal that they tend to concentrate at gap edges for planet masses between $\sim 0.03 M_J$ and $5 M_J$, with M_J being the mass of Jupiter (Fouchet et al. 2007; Owen 2014; Zhu et al. 2014; Gonzalez et al. 2015b; Picogna & Kley 2015). These accumulations are of great interest not only because they could facilitate planetesimal formation, but also because they could supply solid material to the planetary atmosphere through deposition of small grains, and hence contribute to the atmospheric opacity, although perhaps only modestly (Ormel 2014). In particular, a Jupiter-mass planet predominantly accretes particles smaller than 10 μm (Paardekooper 2007), which places a tight constraint on its solid enrichment.

One aspect of the evolution of dust in the vicinity of a gap-opening planet that has not yet been considered is the manner in which solid aggregates arrange themselves. The porosity of dust particle structures affects their aerodynamic coupling to the disk gas. This determines their relative velocities, which in turn influence particle aggregation rates. Crucially, their structure can also affect the ionization state of the protoplanetary disk: the increased surface area associated with internal voids within the dust aggregates allows for efficient sticking of electrons and ions, lowering the ionization levels of the gas phase, and thus rendering the disk gas stable to magnetorotational instability (MRI; Balbus & Hawley 1991), which is a likely candidate to produce turbulent viscosity in disks (although other mechanisms have been proposed to transfer a protoplanetary disk's angular momentum, such as centrifugally driven winds and jets (Blandford & Payne 1982) and magnetic breaking (Matsumoto & Tomisaka 2004)).

Dust in the vicinity of a gap-opening planet is subject to a dynamic and energetic environment. For example, inside the gap, shocks are generated when streams of gas flow through the L1 and L2 points toward the interior of the planet's Hill sphere (Lubow et al. 1999). These shocks can modify the crystalline structure of silicates through thermal annealing. Knowledge of the porous structure of a dust aggregate is essential for determining its heat conductivity during these events.

Previous studies of dust coagulation and dust charging in protoplanetary disks show that electric charges lead to larger, more massive, and more porous aggregates than in the case of neutral coagulation (Matthews et al. 2012). In turn, the evolution of the aggregate porosity may define a region in weakly ionized disks where the growth of sub-micron-sized particles becomes stalled due to electrostatic repulsion between negatively charged aggregates (Okuzumi et al. 2011). Porous aggregates collect more charge than spherical grains of equivalent mass (Ma et al. 2013), and thus the porosity and spatial density of the dust can have a significant effect on MRI turbulence.

The dusty ingredient in the MRI recipe may also be crucial for the dynamics of giant-planet circumplanetary disks. Turner et al. (2014b) showed that under some circumstances, the circumjovian disk has sufficient electrical conductivity for magnetic forces to drive accretion stresses. However, if the disk

contains enough dust, MRI turbulence is unlikely to occur, even in the presence of ionizing X-ray radiation. The circumjovian disk can then develop a substantial magnetically inactive "dead zone," where regular satellites could form.

It is thus evident that the size and internal structure of dust aggregates are key to understanding the birth environments of planets which are capable of opening gaps. To better characterize the spatial distribution of these dust properties around one such planet, in this study we combine a numerical model of MRI turbulence with a dust-coagulation algorithm. Our results will provide a clearer picture of the dust aggregate structures forming around a young, Jupiter-mass planet. In the interest of specificity, we use our models to invoke a scenario in which Jupiter underwent migration within the primitive solar nebula, i.e., the so-called Grand Tack hypothesis (Walsh et al. 2011). According to this hypothesis, Jupiter migrated from inside its current position (but beyond the main asteroid belt) to a distance of about 1.5 au from the Sun, where it encountered an orbital resonance with the trailing Saturn. Both planets then reversed their orbital motion outward. The Grand Tack helps to reproduce the formation of Mars analogs with the correct mass from a disk of planetary embryos.

In Section 2, we describe our numerical models for an MRI-active disk and for dust coagulation, including the effects of porosity and dust compaction. Section 3 presents the results of dust growth driven by MRI turbulence. In Section 4, we discuss these results, and we provide our concluding remarks in Section 5.

2. METHOD

2.1. Disk Model

We use a magnetohydrodynamic (MHD) protoplanetary disk model in the local shearing box approximation (Hawley et al. 1995), in which the MHD equations are solved in a rectangular coordinate system that corotates with the disk at a fiducial orbital radius R_0, with angular frequency $\Omega(R_0)$. In this system, the x axis is oriented along the radial direction, the y axis along the azimuthal direction, and the z axis is parallel to the disk's angular momentum vector. Our solver is the Athena code (Stone et al. 2008), a grid-based algorithm that has been extensively tested and employed for various studies of protoplanetary disks.

Our numerical setup is similar to that of Zhu et al. (2013): the local, three-dimensional (3D) disk model is isothermal and does not include vertical stratification of the gas density. The box dimensions are $16\,H \times 16\,H \times H$, where H is the disk scale height. We use a numerical resolution twice as large as that in Zhu et al. (2013), namely, 64 grid cells per H. In the code's system of units, the gas sound speed c_s, the initial gas density ρ_0, and the angular frequency Ω are all equal to 1. The initial magnetic field strength is given by the plasma beta (the ratio of gas pressure to magnetic pressure), $\beta = 400$, and the initial field configuration corresponds to a non-zero net vertical magnetic flux.

Here, we assume ideal-MHD conditions in which the gas is sufficiently ionized to be perfectly coupled to the magnetic field. In this case, we are ignoring non-ideal terms in the MHD equations that describe Ohmic resistivity, Hall drift, and ambipolar diffusion. These terms would arise as a result of collisions between charged and neutral particles, decoupling the motion of the gas and field (Turner et al. 2014a). Furthermore, the effect of dust grains on the development of MRI turbulence is crucial, since they can remove electrons from the gas and lower its ionization level, preventing the onset of MRI. This, of course, would in turn influence the dust dynamics. Such effects are the ultimate goal of this research. Here, the coagulation of dust particles without charge or feedback to the MRI is modeled as a baseline for future experiments.

To model the gravitational effect of a planet on the surrounding disk gas, we place a cylindrical potential at the center of the box, with an axis coincident with the box's vertical axis. As in Zhu et al. (2013), the planet potential is given by

$$\Phi_{\rm p} = -GM_{\rm p}\frac{r^2 + 1.5r_{\rm s}^2}{(r^2 + r_{\rm s}^2)^{3/2}}, \tag{1}$$

where G is the gravitational constant, $M_{\rm p}$ is the planet mass, r is the distance to the z axis, and $r_{\rm s}$ is a smoothing length used to avoid small time steps close to the source. The potential is also smoothed out to take into account discontinuities at the box boundaries:

$$\Phi_{\rm p,s}(r) = \begin{cases} \Phi_{\rm p}(r_f) - \sqrt{[\Phi_{\rm p}(r_f) - \Phi_{\rm p}(r)]^2 + G^2M_{\rm p}^2/r_{\rm co}^2}, & \text{if } r < r_f \\ \Phi_{\rm p}(r_f) - GM_{\rm p}/r_{\rm co}, & \text{if } r > r_f, \end{cases} \tag{2}$$

where r_f is the cutoff distance to the z axis beyond which the potential flattens out, and $r_{\rm co}$ is a smoothing length at the cutoff radius. Following Zhu et al. (2013), we set $r_f = 7.5\,H$ and $r_{\rm co} = 50\,H$.

In Athena, we express the planet mass in terms of the so-called thermal mass $M_{\rm th}$, the mass at which the Hill radius and the Bondi radius of the planet are comparable to the disk scale height (Rafikov 2006). For the minimum-mass solar nebula model (MMSN; Hayashi 1981) and a solar-mass central star, the thermal mass is (Dong et al. 2011)

$$M_{\rm th} \approx 0.038\left(\frac{c_{\rm s}}{1\ {\rm km\ s^{-1}}}\right)^3\left(\frac{R_{\rm p}}{1\ {\rm au}}\right)^{3/4} M_{\rm J}, \tag{3}$$

where $c_{\rm s}$ is the sound speed in the disk, $R_{\rm p}$ is the planet's semi-major axis, and $M_{\rm J}$ is the mass of Jupiter. Within the Grand Tack scenario, Jupiter begins its inward migration at ~3.5 au, reaches 1.5 au, and reverses its motion toward its current orbital position at 5.2 au (Walsh et al. 2011). Since we are not modeling the actual migration, but effectively only a "snapshot" of that process, we choose $R_{\rm p} = 3$ au because it is an interesting region of the solar nebula in terms of the dynamical evolution of chondritic parent bodies (Walsh et al. 2011). In that case, from Equation (3), one Jupiter mass corresponds to $\approx 6.64 M_{\rm th}$. This is the value of $M_{\rm p}$ that is used in Equation (1) by Athena.

We run this high-resolution setup for 51 orbits (265 year at 3 au in the MMSN) and use the resulting data from the last 12 orbits, after the gas flow reaches an approximate steady state, as input to the coagulation code described next.

2.2. Dust Coagulation Model

Our treatment of dust coagulation follows the implementation of Ormel et al. (2007), which in turn is based on the Monte Carlo model by Gillespie (1975). A population of N particles (we refer to monomers and aggregates jointly as particles) is assumed to be uniformly distributed inside an abstract volume V. The collision rate between particles i and j is calculated as

$$C_{ij} = \sigma_{ij}\Delta v_{ij}/V, \tag{4}$$

where $\sigma_{ij} = \pi(a_i + a_j)^2$ is the collision cross-section, a_i and a_j are the respective particle radii, and Δv_{ij} is the relative speed between the two particles (described below). In this coagulation algorithm, we track the radius of any particle k, a_k, through the enlargement factor $\psi_k = \mathcal{V}_k/\mathcal{V}_0$, where $\mathcal{V}_k$ is the extended volume of the particle (i.e., the volume corresponding to the geometric cross-section of the aggregate[1], which is *not* that of a sphere) and $\mathcal{V}_0$ is the volume of a monomer of radius a_0. We then have $a_k = a_0\psi_k^{1/3}$. We also track the evolution of the particle mass m_k, which is the sum of the masses of the constituent monomers.

Equation (4), together with the sums

$$C_i = \sum_{j=i+1}^{N} C_{ij}, \qquad C_{\rm tot} = \sum_i C_i, \qquad i = 1,\ldots,N-1 \tag{5}$$

defines the probability density $P(i, j, t)$ that particles i and j $(i < j)$ will collide in the time interval $(t, t + dt)$. This probability density function is given by (Gillespie 1975)

$$P(i, j, t) = C_{ij}\exp(-C_{\rm tot}t). \tag{6}$$

We follow the "full-conditioning method" of Gillespie (1975), in which the time interval between collisions is randomly chosen. Our collisions occur at variable intervals Δt given by

$$\Delta t = \frac{1}{C_{\rm tot}}\ln\left(\frac{1}{s_1}\right), \tag{7}$$

where s_1 is a random number chosen from the uniform distribution in the unit interval. The data output from Athena (which includes gas density, gas turbulent velocity, and turbulent stresses) is obtained every orbit, but we interpolate the values of the output variables at 1.2×10^{-4}-orbit intervals using cubic spline interpolation. The time step given by Equation (7) then tells the coagulation code at which times in the sequence of interpolated values a collision should be performed, and the turbulent gas parameters at that time are used to determine the collision rates C_{ij}.

The particle pair (i, j) that will be involved in each collision is also chosen using random numbers, as well as partial sums of the collision rate C_{ij}. The first particle (i) to be involved in the collision is determined by choosing a random number s_2 from the uniform distribution in the unit interval; the random integer i is that for which

$$\sum_{i'=1}^{i-1} C_{i'} < s_2 C_{\rm tot} \leqslant \sum_{i'=1}^{i} C_{i'}. \tag{8}$$

[1] The extended volume is proportional to the total projected cross-sectional area of the particle, $\mathcal{V}_k \sim A^{3/2}$.

Finally, the second particle to collide (j) is chosen by selecting a third random number s_3, also drawn from the uniform distribution in the unit interval, and taking j such that

$$\sum_{j'=i+1}^{j-1} C_{ij'} < s_3 C_i \leqslant \sum_{j'=i+1}^{j} C_{ij'}, \tag{9}$$

with i determined from (8).

In this scheme, for simplicity, we treat three possible outcomes of a binary collision: particles either stick without further restructuring (e.g., when the kinetic energy of collision E is less than the critical energy $E_{\rm comp}$ to initiate compaction); are compacted at the expense of internal voids (i.e., when $E_{\rm comp} < E < E_{\rm maxc}$, where $E_{\rm maxc}$ is the energy at which aggregates are maximally compressed); or bounce off each other ($E > E_{\rm maxc}$; see, e.g., Ormel et al. 2007).[2] The resulting particle is stored in the ith slot. In order to avoid ending up with only one large particle at the end of the calculation, the total number of particles is conserved after a collision takes place. To achieve this, we randomly choose one of the remaining $N - 1$ particles (except j) and we duplicate it. The duplicate is stored in slot j. The partial sums C_i are then updated by subtracting the C_{ij} terms that involve the two particles that just collided, and adding new C_{ij} terms involving the newly formed aggregate and the duplicated particle. Furthermore, the duplication procedure requires that the volume V be increased to preserve the spatial density of dust, $\rho_{\rm d} = \sum_i m_i/V$.

The enlargement factor of a growing aggregate k is calculated according to (Ormel et al. 2007)

$$\psi_k = \frac{m_i\psi_i + m_j\psi_j}{m_i + m_j}\left(1 + \frac{m_j\psi_j}{m_i\psi_i}\right)^{0.425} + \frac{m_j}{m_i}\psi_i e^{-\mu_{ij}/m_{\rm F}}, \tag{10}$$

in the case of pure sticking, with μ_{ij} being the reduced mass of the colliding particles and $m_{\rm F} = 10m_0$, where m_0 is the average mass of a monomer. If the relative velocity of the colliding grains is great enough that the energy exceeds $E_{\rm comp}$, then the collision results in compaction, in which case

$$\psi_k = 1 + \left(1 - \frac{E}{E_{\rm maxc}}\right)\left(\frac{m_i\psi_i + m_j\psi_j}{m_i + m_j} - 1\right). \tag{11}$$

Finally, if bouncing takes place ($E > E_{\rm maxc}$), the enlargement factor is left unchanged. This likely results in an overestimation of the aggregate porosity, which we therefore do not address for bouncing events.

The relative speed Δv_{ij} in Equation (4) has contributions from Brownian motion, $\Delta v_{ij}^{\rm B} = (8k_{\rm B}T\mu_{ij}/\pi)^{1/2}$, where $k_{\rm B}$ is Boltzmann's constant and T is the gas temperature, and from

[2] One important collisional outcome, fragmentation, is not included in our algorithm. This is justified by the fact that the energy needed for the fragmentation of an aggregate that has $N_{\rm mon}$ monomers is $\sim 10^3 N_{\rm mon}$ times larger than the collisional energies of our (small) particles, whose masses and relative speeds during the course of our simulation, which spans a very short time of the disk's dynamical evolution, remain too low for break up (see, for example, Equation (8) of Dominiki & Tielens 1997 for the energy $E_{\rm break}$ needed to break a bond between two monomers; the fragmentation energy is $E_{\rm frag} \simeq N_{\rm mon}E_{\rm break}$ (Ormel et al. 2007)). Upcoming coagulation calculations that make use of an MHD disk model which spans longer timescales will incorporate fragmentation.

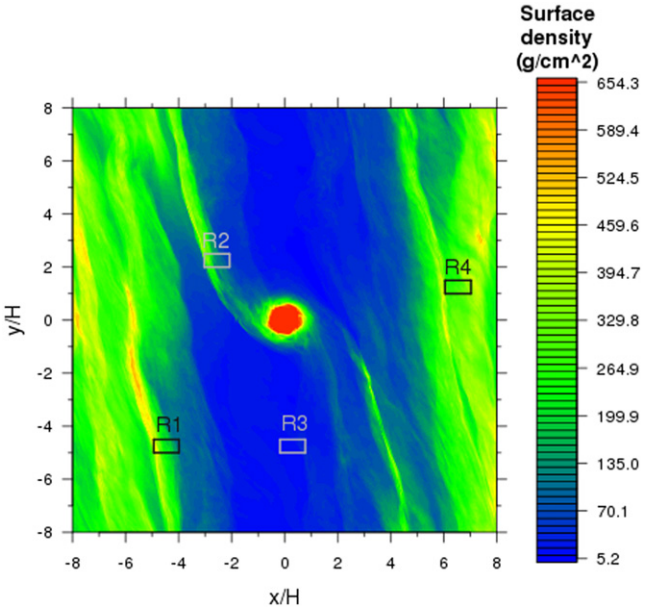

Figure 1. Gas surface density at the end of the MHD simulation ($t = 51$ orbits, or 265 year at 3 au in the MMSN), obtained by averaging the gas density over the vertical extent of the shearing box. The rectangles labeled R1 through R4 mark the box locations from which gas velocities, densities and stresses are fed to the Monte Carlo coagulation code.

turbulence (Ormel et al. 2008),

$$\left(\frac{\Delta v_{ij}^{\mathrm{T}}}{v_{\mathrm{g}}}\right)^2 = \begin{cases} \mathrm{Re}^{1/2}\,(St_i - St_j)^2, & \text{if } t_{\mathrm{s},i} < t_{\mathrm{se}}, \\ \left[2y_a - (1+\epsilon) + \dfrac{2}{1+\epsilon}\right. & \\ \left.\times\left(\dfrac{1}{1+y_a} + \dfrac{\epsilon^3}{y_a+\epsilon}\right)\right]St_i, & \text{if } 5t_{\mathrm{se}} \simeq t_{\mathrm{s},i} \lesssim t_{\mathrm{Le}}. \end{cases} \tag{12}$$

The range of relative speeds Δv_{ij} that we expect to obtain is $\sim$1–10^3 cm s^{-1}. In Equation (12), v_{g} is the gas turbulent speed; $\mathrm{Re} = \nu_{\mathrm{T}}/\nu_{\mathrm{m}}$ is the flow's Reynolds number, with ν_{T} and ν_{m} being the turbulent and molecular viscosities, respectively (the latter is given by $\nu_{\mathrm{m}} \approx c_{\mathrm{s}}\lambda/2$, where λ is the molecular mean free path, as calculated in Cuzzi et al. 1993); $St_k = t_{\mathrm{s},k}/t_{\mathrm{Le}}$ is the Stokes number of particle k, with $t_{\mathrm{s},k}$ being its aerodynamic stopping time (which depends on its radius a and on the gas density ρ_{g}) and t_{Le} the turnover time of the largest turbulent eddies, approximated by the reciprocal of the disk angular frequency Ω; $t_{\mathrm{se}} = \mathrm{Re}^{-1/2}\,t_{\mathrm{Le}}$ is the turnover time of the smallest eddies; $y_a = 1.6$; and $\epsilon \equiv t_{\mathrm{s},j}/t_{\mathrm{s},i} \leqslant 1$.

We obtain the values of the gas turbulent velocity v_{g}, turbulent viscosity ν_{T} (which is given by magnetic and hydrodynamic stresses), and gas density ρ_{g} from the MHD simulation described above. These values are taken from four different regions in the vicinity of the planet, as shown in Figure 1, which portrays the system at the end of our MHD simulation. The figure shows the gas surface density, which is obtained by averaging the gas density over the vertical extent of the box. The gap opened by the planet is clearly defined. The regions R1 through R4 are each divided into 128 subregions of 4×4 grid cells each. We call these subregions macrocells. The gas variables are averaged inside each macrocell, and are then fed to the Monte Carlo coagulation code. Note that although the volume V where each particle population resides is effectively *associated* with each macrocell, it is *not* the volume of the macrocell. The particles do not have position coordinates associated with them.

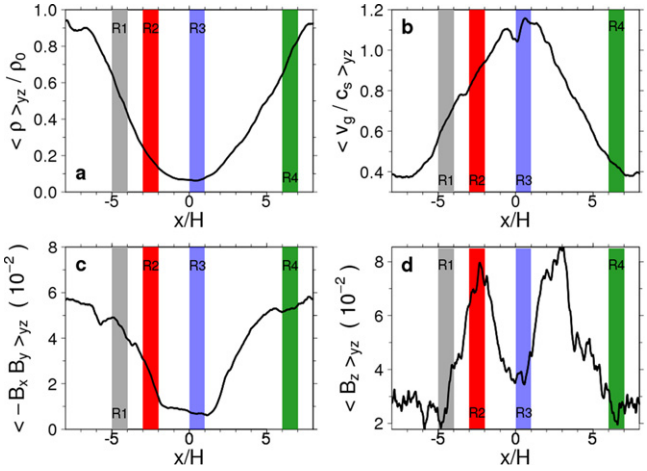

Figure 2. Radial profiles of (a) gas density normalized by its initial value, (b) gas turbulent velocity in units of the sound speed c_{s}, (c) x–y component of magnetic stress tensor, and (d) vertical component of magnetic field. All profiles are time as well as y and z averages. Vertical bars denote the radial position of the reference regions in Figure 1.

We set the number of particles N in the volume V to 10^4, and we use two different initial conditions for the particle sizes: $a_0 = 1$ μm, and a_0 distributed according to the Mathis–Rumpl–Nordsieck (MRN) distribution of dust grains in the interstellar medium, $n(a_0) \propto a_0^{-3.5}$ (Mathis et al. 1977). In the latter case, the range of monomer radii is 0.5 μm $< a_0 <$ 10 μm. In both cases, the monomer bulk density is $\rho_{\mathrm{b}} = 3$ g cm^{-3}. Note that we model micron-sized particles, as opposed to those with millimeter sizes that have been detected in disks with gaps (e.g., Gonzalez et al. 2015a) because micron-sized aggregates play a decisive role in quenching the MRI, and characterizing the structure of micron-sized aggregates is our first step toward future resistive MHD calculations.

Our first set of coagulation calculations (Set 1) are performed with only particle sticking and compaction. In a second set (Set 2), we add the effect of bouncing.

3. RESULTS

Figure 2 shows radial profiles of various quantities associated with the MHD flow. These quantities have been averaged over time (the last 12 orbits of the simulation) and over the y and z directions (excluding the regions for which $|y| < 1$). The vertical bars mark the radial position of the reference regions. In Figure 2(a), the gas density, normalized by the initial density, exhibits a drop of a factor of $\sim$10 inside the gap opened by the planet with respect to the surrounding gas. Panel (c) shows a corresponding factor of 8 drop in the Maxwell stress, which is the main contributor to the turbulent viscosity in accretion disks (Hawley et al. 1995). Figure 2(b) shows the turbulent gas velocity in units of the gas sound speed. Overall, the turbulent gas speeds are relatively high, reflecting the turbulent strength for our case of a non-vanishing initial magnetic flux. Finally, Figure 2(d) reveals that the mean vertical magnetic field has two maxima at either side of the planet's radial position, close to the gap edges. This is in

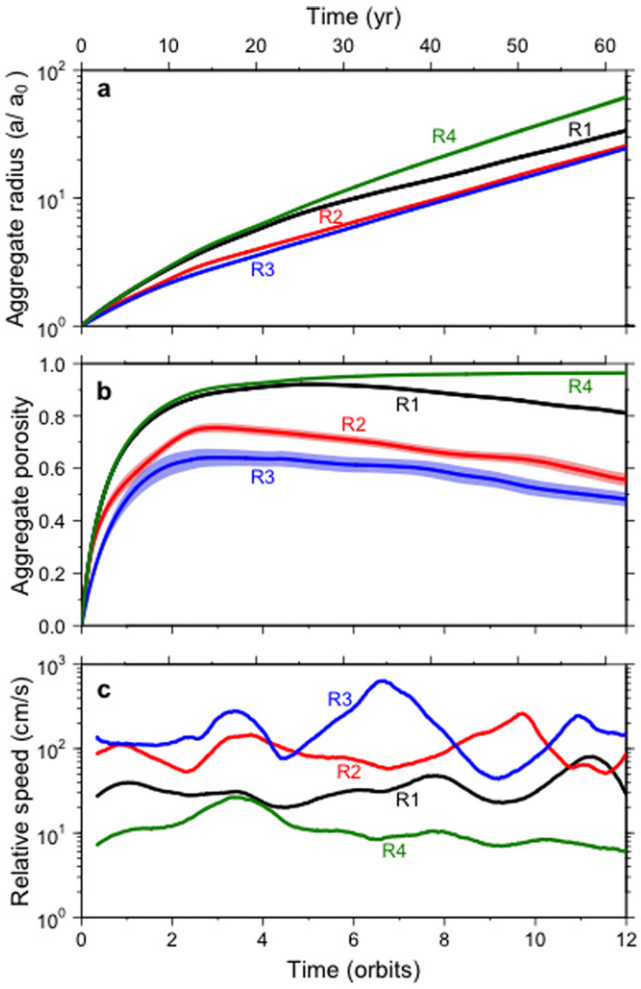

Figure 3. Time evolution of (a) mean aggregate radius $\langle a \rangle$, normalized by the initial monomer radius a_0, (b) mass-weighted average aggregate porosity, and (c) simple moving average (SMA) of relative speed between the two particles involved in each collision, for the monodisperse case. The SMA is taken every 0.35 orbits. Each curve color represents the region Rn ($n = 1,\ldots,4$) of Figure 1 in which coagulation was calculated. In panels (a) and (b), the bands surrounding the solid lines denote one standard deviation of the data taken over the 128 macrocells of each region.

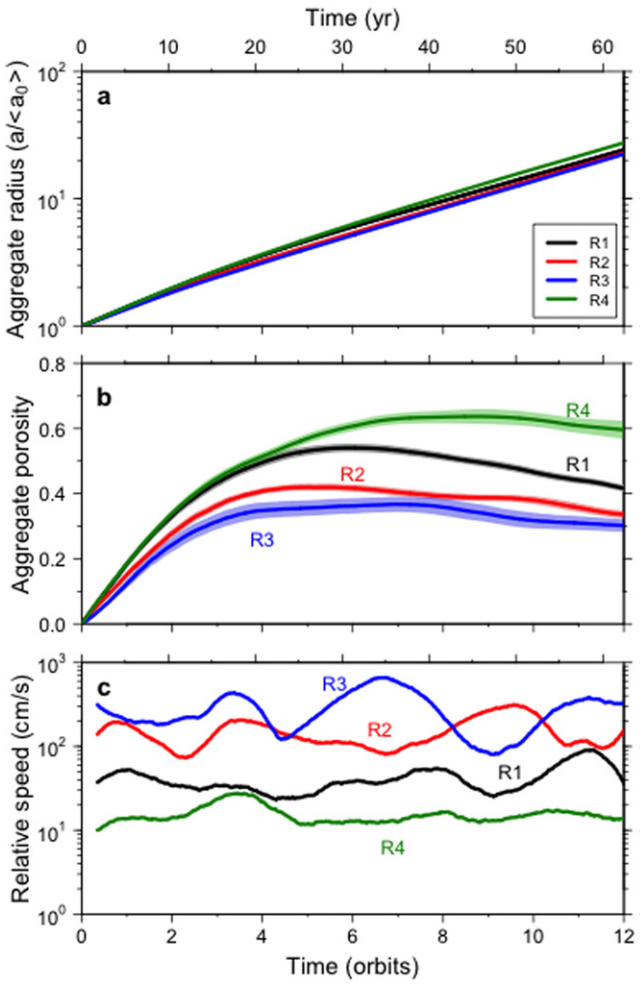

Figure 4. As in Figure 3, but for an MRN-type initial dust size distribution. In panel (a), the mean aggregate radius is normalized by the mean initial monomer radius.

contrast to the centrally peaked profile of $\langle B_z \rangle_{yz}$ measured by Zhu et al. (2013), for a lower planet mass of $1 M_{\rm th}$ ($\approx 0.15 M_{\rm J}$ at 3 au in the MMSN), modeled with half the numerical resolution.

3.1. Set 1: Sticking and Compaction Only

The coagulation evolution of the particle populations with an initial monomer radius of 1 μm is shown in Figure 3. Each curve color refers to one of the four regions identified in Figure 1. Figure 3(a) shows the mean radius of the aggregates, normalized by the initial monomer radius $a_0 = 1\,\mu$m. Growth by sticking occurs slightly more effectively for grains which are subject to the flow conditions in region R4 outside the gap (green curve) where gas velocities are relatively low, as can be seen in Figure 2(b). In comparison, the initial compaction of particles in regions R1, R2, and R3 (black, red, and blue curves, respectively), where turbulent gas velocities are higher, leads to aggregates that are smaller by a factor of ~2. Growth is generally slower in region R1 at the edge of the gap, compared to regions R2 and R3.

The evolution of porosity, defined by the mass-weighted average enlargement factor $\langle \psi_k \rangle_m$ as $1 - 1/\langle \psi_k \rangle_m$ (see Equations (10) and (11)), is shown in Figure 3(b). The compaction of aggregates in regions R2 and R3 is evident, and can be best understood by looking at the relative impact speeds of the aggregate pairs involved in each collision, as shown in Figure 3(c). The highest relative speeds are generated within the gap, as expected from the magnitude of the gas velocity there (Figure 2(b)).

The case of an initial MRN-type size distribution is qualitatively similar to the monodisperse case. Figure 4(a), which also displays the mean particle radius, shows that aggregates in all four regions grow at practically the same rate and achieve very similar sizes. The resulting dusty structures (Figure 4(b)) are slightly more compact than in the monodisperse case, with final porosities in region R3 of 30%, compared to 48% in the same region when $a_0 = 1\,\mu$m.

Since we do not include fragmentation, small grains are not replenished and are removed by the coagulation process. This is evident from the distributions of grain size obtained at the end of the calculations, as shown in Figure 5. The upper panel corresponds to the initially monodisperse dust population, while the lower panel depicts the case of the initial MRN-type size distribution. The colors represent the same regions as in

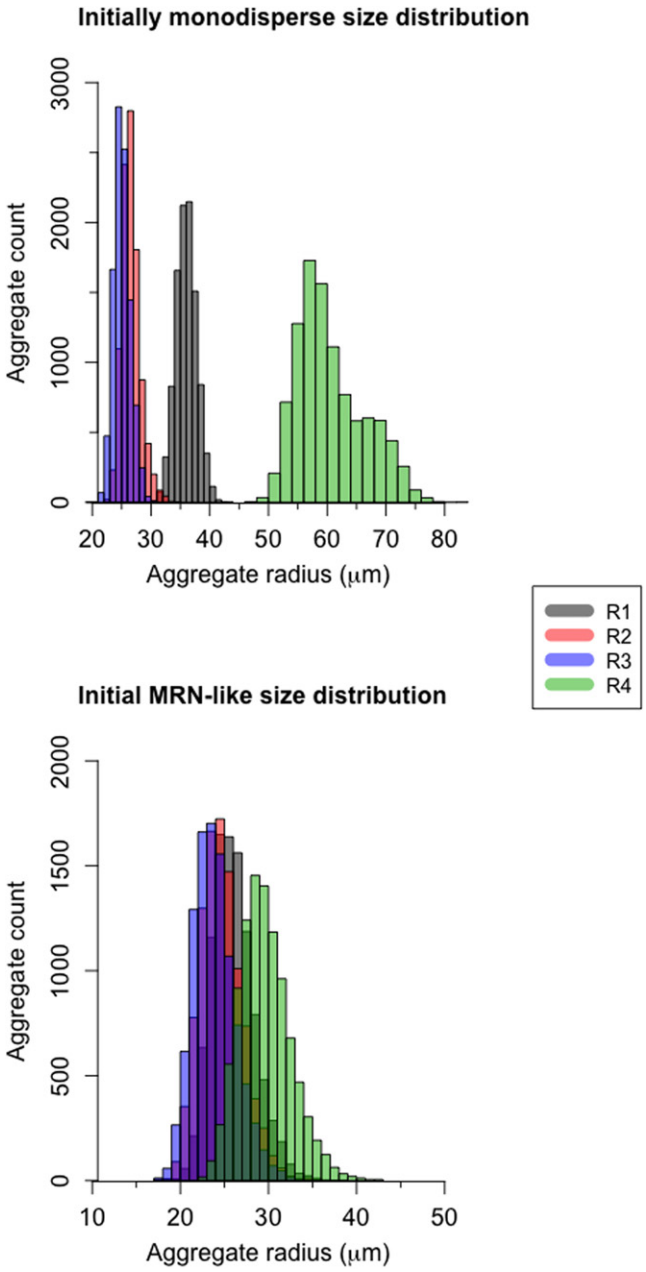

Figure 5. Distribution of dust aggregate radii at the end of the coagulation calculations. The upper panel corresponds to the initially monodisperse dust population, and the lower panel to the population with an initial MRN-like size distribution. The histogram colors represent the same regions as in Figures 3 and 4.

Figures 3 and 4. It is worth bearing in mind that our MHD simulation, and hence the coagulation calculation, spans a very small fraction of the disk lifetime, and therefore these distributions will likely change on longer timescales.

3.2. Set 2: Sticking, Compaction, and Bouncing

We have also added the effect of bouncing to the previous calculations. Note that bouncing collisions result in no aggregate growth, and our implementation of bouncing, by itself, does not take into account the compaction that would result from a bouncing collision (although the compaction resulting from sticking still operates). The results are shown in Figures 6 and 7. One difference that arises with bouncing is that

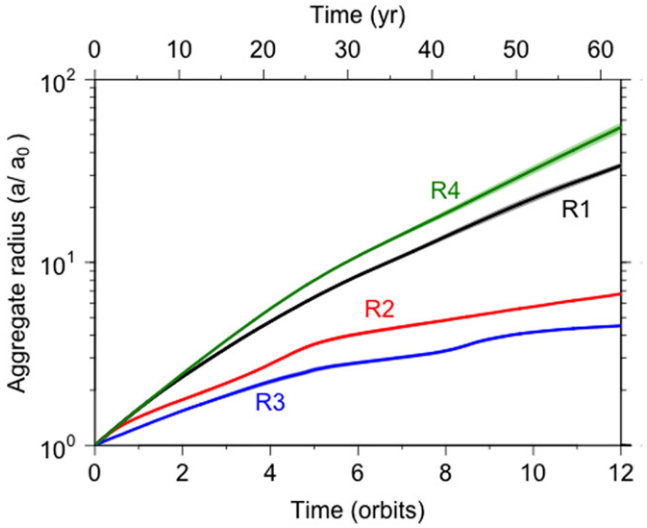

Figure 6. Aggregate radius as a function of time, including the effects of bouncing (coagulation Set 2), for an initially monodisperse size distribution.

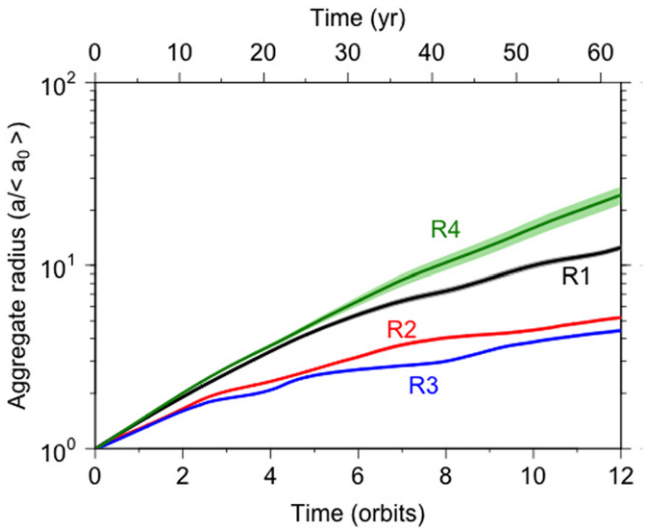

Figure 7. Aggregate radius as a function of time, including the effects of bouncing (coagulation Set 2), for an initial MRN distribution.

aggregate radii in regions R2 and R3 (planetary wake and gap interior, respectively) grow more slowly than in the no-bouncing case. For example, in the gap interior, the inclusion of bouncing collisions produces aggregates which are ∼6 times smaller than in the case where collisions result in perfect sticking, regardless of initial size distribution (Figures 6 and 7).

4. DISCUSSION

Our results indicate that growth by sticking occurs most effectively outside the gap (region R4) where the gas density is higher and the gas turbulent velocity is lower (Figures 2(a) and (b)). In this region, we also found that the mean vertical component of the magnetic field, B_z, is relatively low (Figure 2(d)).

Region R2, located in one of the two planetary wakes, is characterized by lower densities than R4, but higher gas velocities. It is interesting that R2 and R3 (the latter is located in the middle of the low-density gap) are two regions where B_z

has a local maximum and a local minimum, respectively, yet the levels of aggregate growth and compaction are similar.

Particle relative velocities due to turbulence (Equation (12)) depend on the gas sound speed through the molecular viscosity $\nu_{\rm m}$ and the Stokes number St (see text following Equation (12)). Since we have assumed an isothermal gas, the sound speed is constant within the domain defined by our shearing box. This is an adequate assumption if we are not concerned with conditions a few scale heights away from the disk midplane. However, during the early epoch of the solar nebula, the Sun was approximately one order of magnitude more luminous than at present, and sunlight absorbed by the nebula and re-radiated into a Jupiter-induced gap would have heated the gap enough to sublimate water ice (Turner et al. 2012). This effect could increase the gas sound speed within the gap, affecting the relative speeds between solid particles. Moreover, a detailed radiative treatment of the gap would constrain the compositional structure of dust aggregates.

The evolution of the aggregate radius exhibits similar trends within Set 1 (no bouncing) and Set 2 (with bouncing). However, in the latter, a clearer distinction of growth between regions R1 and R4, on the one hand, and regions R2 and R3 on the other, can be seen (Figures 6 and 7). This is due to higher turbulent gas velocities in R2 and R3 that drive the particle relative velocities, which result in more bouncing events, and therefore less growth, than in R1 and R4.

Protoplanetary disks contain a significant amount of millimeter-sized dust grains (Testi et al. 2014; Pinte et al. 2016). It is reasonable to assume that these evolved from interstellar (sub)micron sizes and that the larger grains reside closer to the disk midplane as a result of vertical settling. As such, understanding the evolution of this population can shed light on processes such as vortex trapping (Zhu & Stone 2014) and dust filtration through gap edges (Zhu et al. 2012). The dust aggregate sizes analyzed in this work are considerably smaller than those of more evolved grains. However, it is important to determine the structural features of such micron-sized solids, particularly since they play a key role in establishing the MHD structure of disks (Turner et al. 2010).

Perhaps the most salient omissions in our MHD calculation are the non-ideal effects caused by the varying ionization fraction of the disk. Magnetic field lines can be easily drawn into the planet-induced gap, and the Hall effect dominates the onset of the MRI depending on the relative orientation between the vertical component of the field and the rotation axis of the disk (Keith & Wardle 2015). Nevertheless, certain combinations of column density, magnetic field strength, and dust content can render the gap susceptible to MRI in the ideal-MHD regime, which we assume here.

As mentioned previously, our use of an orbital radius of 3 au for a Jupiter-mass planet is consistent with the Grand Tack hypothesis, allowing our MHD gap model to represent a snapshot of the Grand Tack scenario. In this setting, it is instructive to look at our calculations of aggregate porosities within the context of the formation of meteorite components. In the CV chondrite Allende, chondrule rims, composed of sub-micron grains, may have accreted with high porosities of 70%–80% (Bland et al. 2011). If Jupiter's migration did indeed occur and was contemporaneous with the formation of meteorite parent bodies, then such high porosities may have occurred outside the gap where turbulent gas velocities were lower. In any case, further exploration of our simulation parameters is needed to determine the effect of varying magnetic field strengths and geometries, a different equation of state, and electrical charging of dust grains. The latter effect could delay the growth of rim-forming grains due to electrostatic repulsion (Okuzumi et al. 2011).

5. CONCLUSIONS

Our Monte Carlo calculations of dust growth in and around a gap opened by a Jupiter-mass planet, in the presence of turbulence generated by the magnetorotational instability, indicate that, if one ignores bouncing, aggregate compaction is effective inside the gap, both near the gap edge and in the planetary wake. This is due to the high turbulent relative speeds between aggregates (in the range $\sim$20–600 cm s^{-1}). In these regions, the relative kinetic energies frequently exceed the minimum energy required for restructuring. The lowest porosities occur inside the gap, with a value of $\sim$48% if the initial size distribution of the population is monodisperse (with the radius of all initial monomers equal to 1 μm), and $\sim$30% if the initial size distribution follows a power law with exponent -3.5, as in the MRN distribution for interstellar dust.

In coagulation Set 1 (no bouncing), the most porous aggregates occur in a high-gas-density region outside the gap where the turbulent relative speeds are lower. In that region, porosities reach extremely high values of $\sim$98% for the initially monodisperse population. In the case of the MRN-type population, the porosity reaches $\sim$63%.

The introduction of bouncing (coagulation Set 2) leads to a noticeable slow-down of aggregate growth in the planetary wake (region R2) and inside the gap (region R3) where turbulent gas velocities are higher. Aggregates outside the gap and close to its edge are $\sim$2–8 times larger than those in R2 and R3.

The coagulation calculations performed here span only 12 orbits in the evolution of the planet–disk system, an extremely short time compared to protoplanetary disk lifetimes of a few million years. Current computational capabilities would allow for a modest increase in the running time of similar MHD simulations, which could then provide additional data for longer calculations of micron-sized grain growth.

The outcome of our MHD model of a planet-induced gap, with the planet's mass equal to the mass of Jupiter, differs noticeably from some of the results obtained by Zhu et al. (2013). In particular, the radial profile of the vertical component of the magnetic field is doubly peaked in our simulation, with one peak at either side of the planet's radial position $x/H = 0$, whereas in the Zhu et al. (2013) study the profile exhibits only one peak at $x/H = 0$, for a planet 6.7 times less massive. Future investigations need to determine the effect of the planetary mass on this radial profile, as the vertical component of the magnetic field plays a key role in the susceptibility of a gap to the MRI (Keith & Wardle 2015).

The aggregation of charged grains has been shown to produce aggregates of greater porosity than neutral grains (Matthews et al. 2012). This has implications for the evolution of the disk. Charged grains require the large relative velocities induced by turbulence in order to overcome the Coulomb repulsion between the grains. Thus, the regions seen to inhibit growth here may indeed allow enhanced growth. On the other hand, porous grains collect more charge than equivalent spheres (Ma et al. 2013). At sufficiently large dust densities,

the associated decrease in the plasma density may quench the MRI-induced turbulence, halting grain growth.

We will address the effect of grain fragmentation and charging in subsequent work, using a more sophisticated numerical scheme to treat the growth of porous dust aggregates. Ultimately, the information on the dust density and charge should be included self-consistently in the MHD code to obtain a full picture of the evolving disk dynamics.

REFERENCES

ALMA Partnership et al. 2015, ApJL, 808, L3
Balbus, S. A., & Hawley, J. F. 1991, ApJ, 376, 214
Birnsteil, T., Ormel, C. W., & Dullemond, C. P. 2011, A&A, 525, A11
Bland, P. A., Howard, L. E., Prior, D. J., et al. 2011, NatGe, 4, 244
Blandford, R. D., & Payne, D. G. 1982, MNRAS, 199, 883
Cuzzi, J. N., Dobrovolskis, A. R., & Champney, J. M. 1993, Icar, 106, 102
Dominiki, C., & Tielens, A. G. G. M. 1997, ApJ, 480, 647
Dong, R., Rafikov, R. R., & Stone, J. M. 2011, ApJ, 741, 57
Fouchet, L., Maddison, S. T., Gonzalez, J.-F., & Murray, J. R. 2007, A&A, 474, 1037
Gillespie, D. T. 1975, JAtS, 32, 1977
Gonzalez, J.-F., Laibe, G., Maddison, S. T., Pinte, C., & Ménard, F. 2015a, MNRAS, 454, L36
Gonzalez, J.-F., Laibe, G., Maddison, S. T., Pinte, C., & Ménard, F. 2015b, P&SS, 116, 48
Hawley, J. F., Gammie, C. F., & Balbus, S. A. 1995, ApJ, 440, 742
Hayashi, C. 1981, PThPS, 70, 35
Keith, S. L., & Wardle, M. 2015, MNRAS, 451, 1104
Kraus, A. L., & Ireland, M. J. 2012, ApJ, 745, 5
Lubow, S. H., Seibert, M., & Artymowicz, P. 1999, ApJ, 526, 1001
Ma, Q., Matthews, L. S., Land, V., & Hyde, T. W. 2013, ApJ, 763, 77
Mathis, J. S., Rumpl, W., & Nordsieck, K. H. 1977, ApJ, 217, 425
Matsumoto, T., & Tomisaka, K. 2004, ApJ, 616, 266
Matthews, L. S., Land, V., & Hyde, T. W. 2012, ApJ, 744, 8
Okuzumi, S., Tanaka, H., Takeuchi, T., & Sakagami, M.-A. 2011, ApJ, 731, 96
Ormel, C. W. 2014, ApJL, 789, L18
Ormel, C. W., Cuzzi, J. N., & Tielens, A. G. G. M. 2008, ApJ, 679, 1588
Ormel, C. W., Spaans, M., & Tielens, A. G. G. M. 2007, A&A, 461, 215
Owen, J. 2014, ApJ, 789, 59
Paardekooper, S.-J. 2007, A&A, 462, 355
Picogna, G., & Kley, W. 2015, A&A, 584, 110
Pinte, C., Dent, W. R. F., Ménard, F., et al. 2016, ApJ, 816, 25
Quanz, S. P., Amara, A., Meyer, M. R., et al. 2015, ApJ, 807, 64
Rafikov, R. R. 2006, ApJ, 648, 666
Stone, J. M., Gardiner, T. A., Teuben, P., Hawley, J. F., & Simon, J. B. 2008, ApJS, 178, 137
Testi, L., Birnstiel, T., Ricci, L., et al. 2014, in Protostars and Planets VI, ed. H. Beuther et al. (Tucson: Univ. Arizona Press), 339
Turner, N. J., Carballido, A., & Sano, T. 2010, ApJ, 708, 188
Turner, N. J., Choukroun, M., Castillo-Rogez, J., & Bryden, G. 2012, ApJ, 748, 92
Turner, N. J., Fromang, S., Gammie, C., et al. 2014a, in Protostars and Planets VI, ed. H. Beuther et al. (Tucson: Univ. Arizona Press), 411
Turner, N. J., Lee, M. H., & Sano, T. 2014b, ApJ, 783, 14
Walsh, K. J., Morbidelli, A., Raymond, S. N., O'Brien, D. P., & Mandell, A. 2011, Natur, 475, 206
Zhu, Z., Nelson, R. P., Dong, R., Espaillat, C., & Hartmann, L. 2012, ApJ, 755, 6
Zhu, Z., & Stone, J. M. 2014, ApJ, 795, 53
Zhu, Z., Stone, J. M., & Rafikov, R. R. 2013, ApJ, 768, 143
Zhu, Z., Stone, J. M., Rafikov, R. R., & Bai, X.-N. 2014, ApJ, 785, 122